Editors' Suggestion

Unconventional Charge-to-Spin Conversion in Graphene/$MoTe_2$ van der Waals Heterostructures

Nerea Ontoso,[1] C. K. Safeer,[1,2] Franz Herling,[1] Josep Ingla-Aynés,[1] Haozhe Yang,[1] Zhendong Chi,[1] Beatriz Martin-Garcia,[1,3] Iñigo Robredo,[4] Maia G. Vergniory,[4,5] Fernando de Juan,[3,5] M. Reyes Calvo,[6,7,*] Luis E. Hueso,[1,3] and Fèlix Casanova[1,3,†]

[1] *CIC nanoGUNE BRTA, 20018 Donostia-San Sebastian, Basque Country, Spain*
[2] *Department of Physics, Clarendon Laboratory, University of Oxford, Oxford, United Kingdom*
[3] *IKERBASQUE, Basque Foundation for Science, 48009 Bilbao, Basque Country, Spain*
[4] *Max Planck Institute for Chemical Physics of Solids, Dresden D-01187, Germany*
[5] *Donostia International Physics Center, 20018 Donostia-San Sebastian, Basque Country, Spain*
[6] *Departamento de Física Aplicada, Universidad de Alicante, 03690 Alicante, Spain*
[7] *Instituto Universitario de Materiales de Alicante (IUMA), Universidad de Alicante, 03690 Alicante, Spain*

(Received 19 July 2022; revised 12 October 2022; accepted 16 November 2022; published 19 January 2023)

Spin-charge interconversion (SCI) is a central phenomenon to the development of spintronic devices from materials with strong spin-orbit coupling (SOC). In the case of materials with high crystal symmetry, the only allowed SCI processes are those where the spin-current, charge-current, and spin-polarization directions are orthogonal to each other. Consequently, standard SCI experiments are designed to maximize the signals arising from the SCI processes with conventional mutually orthogonal geometry. However, in low-symmetry materials, certain nonorthogonal SCI processes are also allowed. Since the standard SCI experiment is limited to charge current flowing only in one direction in the SOC material, certain allowed SCI configurations remain unexplored. Here, we perform a thorough SCI study in a graphene-based lateral spin valve combined with low-symmetry $MoTe_2$. Due to a very low contact resistance between the two materials, we can detect SCI signals using both a standard configuration, where the charge current is applied along $MoTe_2$, and a recently introduced [three-dimensional- (3D) current] configuration, where the charge-current flow can be controlled in three directions within the heterostructure. As a result, we observe three different SCI components, one orthogonal and two nonorthogonal, adding valuable insight into the SCI processes in low-symmetry materials. The large SCI signals obtained at room temperature, along with the versatility of the 3D-current configuration, provide feasibility and flexibility to the design of the next generation of spin-based devices.

DOI: 10.1103/PhysRevApplied.19.014053

I. INTRODUCTION

Since its discovery in 2004, graphene has become a platform to investigate physical phenomena [1,2]. Its isolation opened the door to the discovery and study of a huge family of two-dimensional (2D) materials that can host a plethora of properties [3–10]. In the field of spintronics, graphene proves to be an ideal candidate to transport spin currents over long distances, due to its low spin-orbit coupling (SOC) [11–14], which, in turn, limits its capability for the manipulation of spin currents. However, SOC can be enhanced in graphene by proximity to another 2D material in van der Waals heterostructures [15–20], leading to weak antilocalization [21–25], spin-lifetime anisotropy [26–28], and enabling electrical control of spin currents [29,30] and of the SOC-induced spin precession [31]. Spin-orbit proximity in graphene also causes the spin Hall effect (SHE) [32–35] and the Edelstein effect (EE) [34–39], giving rise to electrically controllable spin-charge interconversion (SCI). This is a crucial ingredient to achieve magnetic-field-free switching [40] and read-out [41,42] of magnetic elements in memory and logic devices.

The spin Hall conductivity tensor, σ, relates the electric field (E), associated with the applied charge current, to the generated spin-current density by $j_i^k = \sigma_{ij}^k E_j$, where i corresponds to the spin-current direction, j to the charge-current direction, and k to the spin-polarization direction. The nonzero components of the tensor determine the allowed geometrical configurations of the SCI due to the SHE. In materials with high crystal symmetry, where at least two mirror planes are present, the only nonzero

*reyes.calvo@ua.es
†f.casanova@nanogune.eu

elements of σ_{ij}^{k} fulfill $i \neq j \neq k$, i.e., charge-current, spin-current, and spin-polarization directions are mutually orthogonal. However, in low-symmetry materials, additional nonorthogonal components are allowed [43–46]. That is the case for the transition-metal dichalcogenide (TMD) $MoTe_2$ in the $1T'$-crystal phase, which is characterized by only one mirror plane (M_a), perpendicular to the Mo chain, which lies along the y direction in the experimental configuration, and a screw axis parallel to it [47]. In this case, when the spin polarization is in plane and perpendicular to the mirror plane (k along the y direction), the σ_{ij}^{k} components for which the spin current is parallel to the applied charge current ($i = j$) are also allowed, giving $\sigma_{ii}^{y} \neq 0$ (see Refs. [46,48]). In addition to the SHE, the EE can also lead to SCI. In SOC materials with broken inversion symmetry, the flow of charge current is expected to generate spin accumulation in the system. In a graphene-based van der Waals heterostructure, this effect can also occur in proximitized graphene [34–37,39]. The symmetries that govern the permitted SCI processes via the EE depend on the mirror alignment between graphene and the SOC material [49–54]. In twisted heterostructures, besides the conventional EE, where the charge current induces a perpendicular spin polarization, the broken mirror symmetry leads to an unconventional EE with parallel spin polarization. Experimentally, such an unconventional EE was recently observed in graphene/$MoTe_2$ [55], graphene/WTe_2 [56], and graphene/$NbSe_2$ [57] heterostructures.

So far, $1T'$-$MoTe_2$ has been studied as a SCI material using nonlocal lateral-spin-valve (LSV) [39,55] and spin-orbit-torque experiments [58,59]. While most artifacts induced by the local charge current are avoided in nonlocal LSVs, the injection of the charge current in the SOC material is limited to one direction, leaving certain SCI configurations unexplored. For SCI experiments using nonlocal LSVs, based on the spin-absorption phenomenon, a versatile measurement geometry is required to study unexplored SCI components. Recently, an alternative measurement configuration, where the charge current propagates in three dimensions (3D) was implemented, leading to the observation of different SCI components in graphene/WTe_2 [60] and graphene/BiTeBr [61] heterostructures. In these studies, the charge current is applied between the SOC material and the graphene channel. These experiments, however, only return a measurable signal when the interface resistance is high enough and spin absorption in the SOC material is suppressed, implying that the simultaneous detection of SCI in the standard and the recently introduced 3D-current configuration cannot be achieved.

Here, we combine the conventional configuration with the recently introduced 3D-current configuration to measure and characterize SCI in a graphene/$MoTe_2$ van der Waals heterostructure. The low interface resistance between graphene and $MoTe_2$ allows us to measure SCI in both configurations in the same device up to room temperature. We discover that spin generation occurs when charge current flows through the $MoTe_2$ flake in any direction, gaining deeper insights into the multidirectional SCI processes in graphene/$MoTe_2$. Whereas the SCI component due to a nonorthogonal arrangement of spin polarization and charge current was measured before [55], additional components due to both orthogonal and nonorthogonal SCI geometries are measured here. Specifically, we detect SCI signals corresponding to the cases where a charge current propagating along the mirror plane [b-crystal axis in Fig. 1(a), which corresponds to the x direction in our space coordinates] or along the vertical stacking (z direction) generates a spin current with the same in-plane orthogonal polarization [a-crystal axis in Fig. 1(a), corresponding to the y direction]. The origin of the former contribution is compatible with the SHE in $MoTe_2$ or the EE in

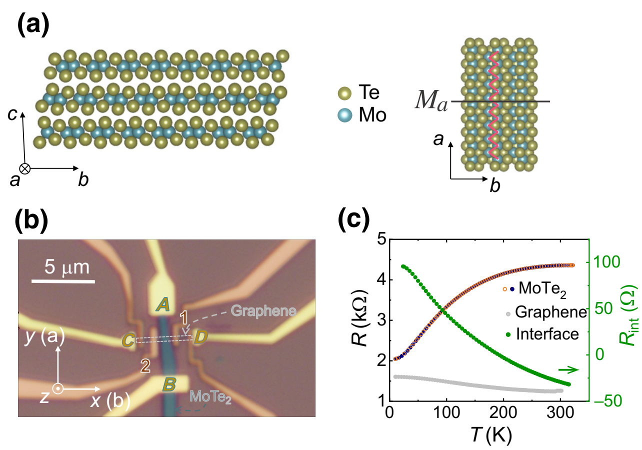

FIG. 1. (a) Sketch of the $MoTe_2$ crystal structure in the $1T'$ phase. This phase is characterized by a tilt of 93.83° in the c-crystal axis and a Mo chain along the a-crystal axis (pink zigzag line). a axis corresponds to the preferential cleaving direction during mechanical exfoliation, giving rise to elongated flakes suitable for the LSV devices. $1T'$ phase hosts a mirror in the b-c plane (M_a) and a screw axis along the b-crystal axis (not represented). (b) Optical microscope image of the device. Barely visible narrow graphene flake along x, represented by the dashed rectangle, is under the $MoTe_2$ flake (blue). Ti/Au electrodes are labeled with letters and FM TiO_x/Co electrodes with numbers. Relationship between the crystal axis and space coordinates is as follows: $b = x$ and $a = y$. It should be noted that the c-crystal axis is not along the z direction. (c) Two-point resistance as a function of temperature of the $MoTe_2$ flake when cooling down (orange open circles) and warming up (blue filled circles), as measured in the $V_{AB}I_{AB}$ configuration. Four-point resistance of the few-layer graphene flake as a function of temperature, as measured in the $V_{21}I_{CD}$ configuration, is also shown (gray circles). Green circles correspond to the interface resistance between graphene and $MoTe_2$, as measured in the $V_{AC}I_{BD}$ configuration.

proximitized graphene, while the SHE in $MoTe_2$ is the only allowed mechanism that explains the unexplored σ_{zz}^{y} SHE component in $MoTe_2$, additionally confirmed using density-functional theory (DFT) calculations. The large SCI signals measured here at room temperature, together with the versatility in the 3D-current configurations, makes $MoTe_2$/graphene heterostructures ideal candidates to be integrated into functional 2D spintronic devices.

II. EXPERIMENTAL DETAILS

The LSV device used for our measurement is shown in Fig. 1(b). The device is similar to those used in a related work by some of the authors [55]. First, an elongated $MoTe_2$ flake of about 20 nm thick—$MoTe_2$ tends to cleave along the Mo chain [55] [pink zigzag line along the *a*-crystal axis in Fig. 1(a)]—is mechanically exfoliated under an inert atmosphere and stamped on top of an exfoliated few-layer graphene flake using the dry-viscoelastic technique [62]. In this way, $MoTe_2$ is not exposed to air, preventing oxidation, and keeping a clean interface between $MoTe_2$ and graphene. The width of the $MoTe_2$ flake on top of the graphene channel is about 1 μm. After stamping, metallic Ti(5 nm)/Au(100 nm) electrodes [labeled with letters in Fig. 1(b)] contacting $MoTe_2$ and graphene are fabricated via *e*-beam lithography, thermal evaporation, and lift-off. Subsequently, ferromagnetic (FM) electrodes [labeled with numbers in Fig. 1(b)], TiO_x(0.3 nm)/Co(35 nm), are fabricated on top of graphene, using the same technique. TiO_x is prepared by air exposure of a Ti layer, as described elsewhere [55]. The width of TiO_x/Co electrodes is approximately 300 and 400 nm on the left and right sides of the $MoTe_2$ flake, respectively.

To characterize our $MoTe_2$ flake, we measure its resistance (R) by applying a current between contacts A and B (I_{AB}) and measuring the voltage between the same electrodes (V_{AB}). We label this geometry as $V_{AB}I_{AB}$. As shown in Fig. 1(c), the resistance of the $MoTe_2$ flake ($R_{AB} = V_{AB}/I_{AB}$) has a temperature dependence compatible with semimetallic behavior [63]. Resistance curves for cooling and heating sweeps perfectly overlap, showing no fingerprint of the structural transition from $1T'$ to $1T_d$ phases [58,64] otherwise reported for the bulk material [65]. This is confirmed by the temperature evolution of polarized Raman spectra (see Ref. [48]). The graphene flake resistance, measured in a four-point configuration ($V_{21}I_{CD}$), is also plotted in Fig. 1(c). The quality of the interface can be inferred by measuring the interface resistance between graphene and $MoTe_2$. By applying a charge current between one side of $MoTe_2$ and graphene (I_{BD}) and measuring the voltage between the other sides (V_{AC}), the interface resistance ($R_{\text{int}} = V_{AC}/I_{BD}$) is probed. As shown in Fig. 1(c), R_{int} shows very low values, even negative at room temperature, and increasing up to 100 Ω at 10 K, meaning that the interface resistance is smaller than the graphene square resistance [55].

III. RESULTS AND DISCUSSION

SCI has been observed in graphene due to the spin-orbit proximity effect. Most of these reported experiments use a LSV based on graphene and a semiconducting high-SOC van der Waals material, in which graphene is shaped into a Hall bar and contacted to probe SCI voltage from the proximitized region [32–39]. However, if graphene is combined with a conducting (metallic or semimetallic) van der Waals material, SCI can be measured by directly probing the voltage across both materials. In this case, disentangling the origin of each SCI process remains challenging, as it can either occur via the EE or the SHE in proximitized graphene [36,39,56,57,66] or in the high-SOC material itself via the SHE [38,55,67,68]. In the standard nonlocal SCI measurement configuration [55,69,70], the charge current (I_c) is applied along the SOC material (y direction). In highly symmetric materials, I_c generates a spin current via the SHE in the vertical direction (z direction) with spin polarization along the x direction (corresponding to the spin Hall conductivity tensor component, σ_{zy}^{x}). The spin current flows into the graphene channel and is detected with a FM electrode as a nonlocal voltage (V_{NL}). To detect the spin current, the magnetization of the FM has to be pulled in the same direction as spin polarization and, thus, the magnetic field is applied along the in-plane hard axis (x direction). When the SOC material has lower crystal symmetry, spin polarization in other directions can also be generated. In the $1T'$-crystal phase, nonorthogonal components are allowed with spins polarized along the Mo chain (y direction, see Ref. [48]). Hence, for this material, it is also of interest to keep the magnetization of the FM along its easy axis (y direction), while the charge current is applied along different directions within the high-SOC material.

A. Standard configuration

We first study SCI by applying the charge current along the $MoTe_2$ flake [i.e., along the y direction, Fig. 2(a)] while sweeping the magnetic field along the FM easy axis (H_y). The nonlocal resistance ($R_{\text{NL}} = V_{\text{NL}}/I_c$) dependence with H_y shows a hysteresis loop with two clear jumps at the switching field of the FM when using contact 2 (on the left side of the $MoTe_2$ flake) as a detector [Fig. 2(b)]. The amplitude of the signal is given by ΔR_{NL}, which, in this case, can only arise from the charge current, I_c, that flows along the $-y$ direction, denoted as I_c^{-y}, either along the $MoTe_2$ flake or along the proximitized graphene. When the magnetization of the FM is positive (negative), R_{NL} takes a lower (higher) value. Hence, the injected spins are polarized along the $-y$ direction. Note that we assume

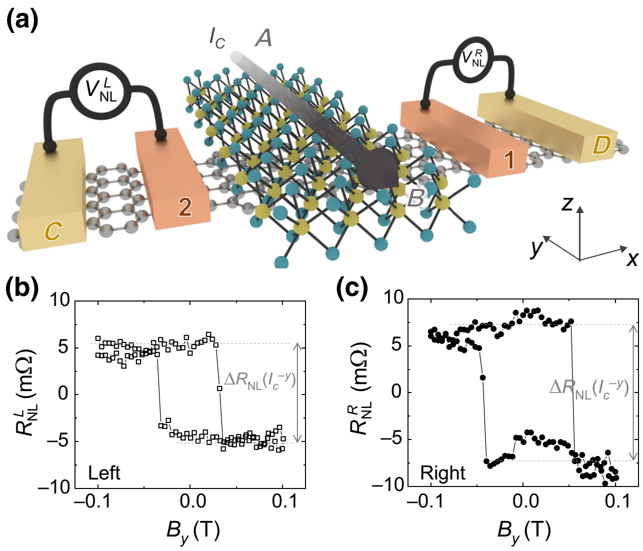

FIG. 2. (a) Sketch of the standard SCI measurement configurations that can be performed in the heterostructure. Charge current (I_c) is applied along $MoTe_2$ and the voltage is probed using the FM electrode on the left or right sides of the $MoTe_2$ flake. (b) Nonlocal resistance (R_{NL}) measured using left Co contact 2 as a detector (V_{NL}^L), while sweeping the magnetic field along the in-plane easy axis (y- direction). (c) Similar measurement using right Co electrode 1 as a detector (V_{NL}^R). Baselines of 110 and 26 mΩ are removed, respectively. All the measurements are performed at 300 K.

that the graphene/FM contact spin polarization is positive. We keep this convention throughout the manuscript. Therefore, we can conclude that a y-spin polarization is generated by applying I_c along the same direction in the $MoTe_2$ flake.

Three possible mechanisms could be behind this spin generation: (i) the EE in proximitized graphene, (ii) the SHE in $MoTe_2$ with a spin current along the z direction, or (iii) the SHE in $MoTe_2$ with the spin current along the x direction. Concerning case (i), spin accumulation polarized along $-y$ must be generated by a perpendicular charge current (x or z direction) in the conventional EE. However, in this case, the charge current and spin polarization are parallel, which is forbidden by the crystal symmetry of graphene. If we consider cases (ii) and (iii), both SHE components (σ_{xy}^y or σ_{zy}^y, respectively) should be zero, since they are forbidden by the crystal symmetries of $MoTe_2$ (see Ref. [48]).

To further understand the possible mechanism, R_{NL} is measured using contact 1 as a detector (on the right side of $MoTe_2$ flake), while the magnetic field is swept along the FM easy axis, as represented in Fig. 2(c), a configuration that probes the spin current flowing in the opposite direction than that using contact 2. ΔR_{NL} shows the same sign as the one detected on the left side. The absence of a sign reversal further proves that the spin current along the x direction does not play any role in SCI. Accordingly, two mechanisms remain as possible origins of the signal: an unconventional SHE in $MoTe_2$ with spin current along the z direction (σ_{zy}^y) or an unconventional EE at proximitized graphene (that does not depend on spin-current directions), where spin polarization and charge current are parallel. Both scenarios are incompatible with the processes allowed by the crystal symmetry of both $MoTe_2$ and graphene.

Therefore, the symmetry of the system must be broken to allow such unconventional SCI. A possible origin for symmetry breaking is shear strain, which may develop during the fabrication process, as suggested in Ref. [58]. However, this signal is now reproduced in several graphene/$MoTe_2$ samples (this work and Ref. [55]) and even in different graphene/TMD heterostructures [56, 57]. Shear strain is expected to be sample dependent [71], making this hypothesis unlikely. Another possible mechanism is that the misalignment between the mirror planes of graphene and $MoTe_2$ creates a nonsymmetric interface. This enables an unconventional EE in proximitized graphene, for which spin polarization is parallel to the charge-current direction [49–54].

B. 3D-current configuration

Up to this point, we have only explored SCI arising from a current flowing along the $-y$ direction (I_c^{-y}). To further access other SCI processes, the current path in $MoTe_2$ must include components along the three different space coordinates. We implement a protocol [38,58,59,66] (which we call 3D-current configuration), where I_c is injected from $MoTe_2$ into graphene through the interface using one Ti/Au electrode on $MoTe_2$ (A or B) and another one on graphene (C or D). In this configuration, I_c propagates along x, y, and z, and spin currents arising from current flowing in all three directions can be detected. To separate their contributions to spin polarization, we test different nonlocal measurement configurations by reversing each x, y, or z component of I_c independently. When one of the components of I_c is reversed, spin polarization and the associated nonlocal voltage in the detector resulting from the charge current must change sign, regardless of the origin of SCI.

The four possible charge-current paths within the graphene/$MoTe_2$ heterostructure when contact 1 is used as the FM detector are sketched in Fig. 3(a). The measured R_{NL} as a function of H_y for each of these current paths is plotted in Fig. 3(b), where hysteresis loops are represented by the same color as the respective current path. In this specific measurement configuration, R_{NL} signals are proportional to the number of y-polarized spins arriving at the detector. In other words, our experimental configuration detects SCI processes that generate y-polarized spins, which may arise from any charge-current propagation

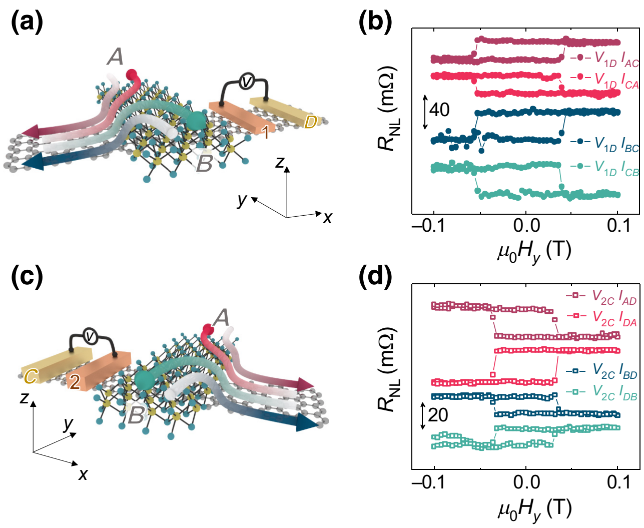

FIG. 3. (a) Sketch of all 3D-current SCI measurement configurations using contact 1 as a FM detector. Arrows across $MoTe_2$/graphene represent the four different current paths. (b) Nonlocal resistance measured using contact 1 as a FM detector, while sweeping the magnetic field along the FM easy axis (H_y) for different current paths. Curves are vertically shifted for clarity. Arrow represents an amplitude of 40 mΩ. (c) Sketch of all 3D-current SCI measurement configurations using contact 2 as a FM detector. (d) Nonlocal resistance measured using contact 2 as the FM, while sweeping the magnetic field along the FM easy axis (H_y) for different current paths. Arrow represents an amplitude of 20 mΩ. All the measurements are performed at 300 K.

direction. To distinguish the charge-current direction creating spin polarization along y, each charge-current path can be spatially decomposed as follows: dark-red path corresponds to I_c ($-x$, $-y$, $-z$), light red to I_c ($+x$, $+y$, $+z$), dark blue to I_c ($-x$, $+y$, $-z$), and light blue to I_c ($+x$, $-y$, $+z$). As shown in Fig. 3(b), dark-red and dark-blue curves show the same hysteresis-loop sign, while light-red and light-blue curves also show the same sign but opposite to that of the dark curves. Considering the correspondence between the signs of the loops and the charge-current directions, we can conclude that the sign change of the R_{NL} signal may arise from a reversal of the charge current along either the x or z direction.

To shed further light on the SCI origin, another set of measurements with the 3D-current configuration is implemented using contact 2 as the FM detector, which allows us to access four extra current paths [see Fig. 3(c)]. Figure 3(d) shows R_{NL} as a function of H_y for the four extra configurations. In this case, decomposition of the charge current is as follows: dark-red path corresponds to I_c ($+x$, $-y$, $-z$), light red to I_c ($-x$, $+y$, $+z$), dark blue to I_c ($+x$, $+y$, $-z$), and light blue to I_c ($-x$, $-y$, $+z$). If we apply the same sign-comparison protocol used for measurements shown in Fig. 3(b), we can again conclude that the R_{NL} signal originates from the charge current along either the x or z direction. To distinguish between these two possible origins, we need to further compare the two sets of measurements shown in Figs. 3(b) and 3(d). Table I contains a summary of the different measurement configurations, the respective spatial components of I_c, and the amplitude of the resulting nonlocal signal loop (ΔR_{NL}) at the detector. It is important to notice that only the I_c component along the x direction is reversed when comparing the two sets of data obtained from detectors 1 and 2. In other words, in the configurations represented by the same color in Figs. 3(a) and 3(c), the charge current follows the same path, except for a reversal in the x direction. If their corresponding same-color R_{NL} signals in Figs. 3(b) and 3(d) are compared, a reverse in the R_{NL} signal is observed for each of the four nonlocal resistance configurations. This implies that it is the charge current along the x direction ($I_c^{\pm x}$) that dominates the generation of spin polarization along the $\mp y$ direction. Hanle spin-precession measurements corroborate the spin origin of the nonlocal signals detected for both the standard and 3D-current measurement configurations [48].

C. Analysis of the signals and discussion of the mechanisms

The possible mechanisms behind SCI with charge current along x and spin polarization along y are the SHE in $MoTe_2$ or the EE in proximitized graphene. For the former, a charge current along the x direction generates a spin current along the z direction with spin polarization along y (corresponding to σ_{zx}^{y}). For the latter, a charge current along x generates a spin accumulation with spin polarization along y. In contrast to the signal measured using the standard SCI configuration (Fig. 2), and regardless of the SHE or EE origin, this signal is allowed by symmetry [48] and has not been detected before.

Using both the standard [Figs. 2(a) and 2(b)] and 3D-current [Figs. 3(a) and 3(c)] SCI measurement configurations in the graphene/$MoTe_2$ heterostructure, we observe how both x- and y-charge-current directions ($I_c^{\pm x}$ and $I_c^{\pm y}$, respectively) induce spins polarized along the y direction. To quantitatively compare them, the amplitude of the SCI signal (ΔR_{NL}), which is defined as the difference between the mean value of the nonlocal resistance at the two saturating states, is extracted for each configuration and shown in Table I. For each FM detector, two configurations result in positive ΔR_{NL}, while the other two show the opposite sign. It is remarkable that the absolute value of the amplitude for the signals with the same sign are not the same. The difference in ΔR_{NL} between the two signals with positive (negative) amplitudes, that is, approximately 10 mΩ in both cases, must arise from SCI of the charge current along the y direction, as discussed next.

From the standard SCI measurement configuration (Fig. 2), we know that there is a SCI signal with spin

TABLE I. Summary of the different measurement configurations carried out in the graphene/$MoTe_2$ heterostructure. For each configuration, the components of I_c with the corresponding symbol in the plot, and the respective amplitude of the signals are detailed.

Configuration	Detector	I_c	ΔR_{NL} (mΩ)
Standard configuration	Contact 1	● $(0, -y, 0)$	−13.6
	Contact 2	□ $(0, -y, 0)$	−9.1
3D-current configuration	Contact 1	● $(-x, -y, -z)$	22.2
		● $(+x, +y, +z)$	−21.8
		● $(-x, +y, -z)$	32.4
		● $(+x, -y, +z)$	−30.7
	Contact 2	□ $(+x, -y, -z)$	−21.4
		□ $(-x, +y, +z)$	24.1
		□ $(+x, +y, -z)$	−13.1
		□ $(-x, -y, +z)$	10.6

polarization along y when the charge current is applied along the $-y$ direction (I_c^{-y}) and ΔR_{NL} of this contribution is negative, being positive when the current flows in the $+y$ direction (I_c^{+y}). In the 3D-current experiments, this contribution to SCI is measured together with the signal coming from the charge current flowing in the x direction. If we compare the dark-blue and dark-red configurations in Fig. 3(a) or Fig. 3(c), the only difference in the charge-current path between them is the direction of the charge current along the y direction. For example, in the case of contact 1 working as a detector [Figs. 3(a) and 3(b)], the dark-blue configuration corresponds to I_c ($-x$, $+y$, $-z$), while the dark-red case corresponds to I_c ($-x$, $-y$, $-z$). Since ΔR_{NL} is positive, we conclude that a charge current along the $-x$ direction (I_c^{-x})generates spin polarization along the $+y$ axis. In contrast, a charge current along the $-y$ direction (I_c^{-y})generates spin polarization along the $-y$ direction, and I_c^{+y} generates spin polarization along $+y$. A similar scenario can be applied to explain the difference between the two negative values of ΔR_{NL} for the light-colored curves. In other words, for each pair of dark or light curves measured at detector 1, the contributions to ΔR_{NL} arising from $I_c^{\pm x}$ and $I_c^{\pm y}$ have the same sign for the blue curves; therefore, they add up. In contrast, for the red curves, the contributions to ΔR_{NL} arising from $I_c^{\pm x}$ and $I_c^{\pm y}$ present the opposite sign, subtracting their values (Fig. 4). By considering the contribution to the amplitude of each hysteresis loop coming from $I_c^{\pm x}$ and $I_c^{\pm y}$, that is, $\Delta R_{NL}(I_c^{\pm x})$ and $\Delta R_{NL}(I_c^{\pm y})$, respectively, the ratio of the absolute values of the SCI signal amplitudes, $\Delta R_{NL}(I_c^{\pm x})/\Delta R_{NL}(I_c^{\pm y})$, can be obtained. A similar analysis is also shown in Fig. 4 for measurements using FM detector 2, as explained in Figs. 3(c) and 3(d).

In another comparison, the amplitude of the signal measured in the standard configuration and using contact 1 as

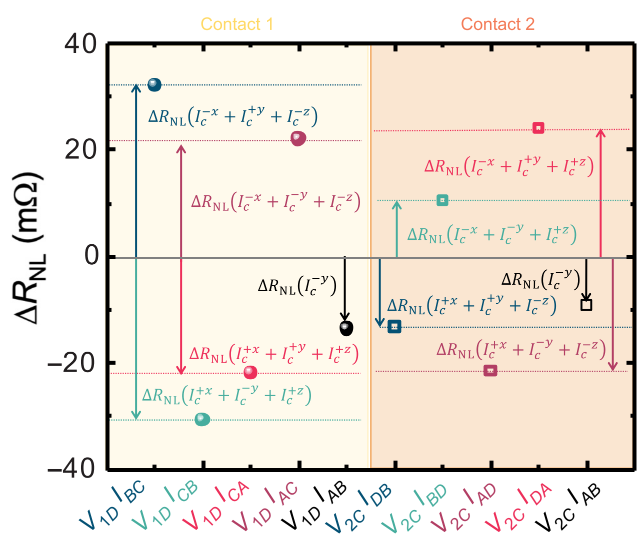

FIG. 4. Amplitude of the SCI signals (ΔR_{NL}) for each of the eight different current paths in the 3D-current configurations and for the standard configuration. Each arrow is labeled with the charge current involved in the SCI process for each measurement. Contact 1 is used as a detector for the five configurations on the left side (light-yellow background), while contact 2 is the detector for the five combinations on the right side (light-orange background). Error bars are smaller than the dots.

the detector is approximately 1.5 times larger than that detected using contact 2 (see Table I). This difference can be attributed to the different degrees of polarization of the two FM electrodes or to the different distances between the detector and the $MoTe_2$ flake. However, in the 3D configuration, we also observe large differences between signals measured with the left and right detectors, which cannot be solely attributed to the different degrees of polarization or different distances to the Co electrodes. If we consider that only x- and y-flowing currents contribute to spin generation, and the difference arises just from polarization or the distance to the FM leads, the ratio $\Delta R_{NL}(I_c^{\pm x})/\Delta R_{NL}(I_c^{\pm y})$ should be the same for both detection schemes. However, this ratio is significantly smaller for detector 2 than for detector 1. Interestingly, and even if we cannot fully discard contributions from geometrical factors or from inhomogeneities in the spin absorption of the $MoTe_2$/graphene interface, the pattern on the differences between detector 1 and detector 2 for the signals can be naturally explained by considering the presence of SCI from $I_c^{\pm z}$. If we now consider that the amplitude of each hysteresis loop comes from the presence of SCI of the spins polarized along y for three charge-current directions, the SCI signal coming from $I_c^{\pm z}$ can be extracted and is comparable to that of $\Delta R_{NL}(I_c^{\pm y})$, being both smaller than $\Delta R_{NL}(I_c^{\pm x})$. $\Delta R_{NL}(I_c^{+z})$ and $\Delta R_{NL}(I_c^{+x})$ show the same sign, opposite to the one of $\Delta R_{NL}(I_c^{+y})$ (Table I and Fig. 4). In this scenario, when using contact 1 as a detector, the contributions of $\Delta R_{NL}(I_c^{\pm x})$ and $\Delta R_{NL}(I_c^{\pm z})$ present the same sign for each situation, enlarging the total amplitude of the hysteresis loop. However, in the case of contact 2, the two contributions present opposite sign, reducing the total amplitude of the SCI signal. The origin of this SCI component arising from $I_c^{\pm z}$ can only be attributed to the SHE in $MoTe_2$, where the charge current is along the z direction, parallel to the spin-current direction, and the injected spins are polarized along the y direction. This configuration corresponds to the σ_{zz}^{y}-tensor element, which is allowed by the crystal symmetry of $1T'$-$MoTe_2$ [48].

By comparing the amplitudes and signs of the different SCI components in our device and assuming the three processes occur via the SHE in $MoTe_2$, we conclude that σ_{zx}^{y} presents the same sign as that of σ_{zz}^{y} and opposite to that of σ_{yz}^{y}, and that σ_{zx}^{y} is larger in magnitude than σ_{zz}^{y} and σ_{yz}^{y}. This hierarchy of components can be compared with that obtained from DFT calculations of the spin Hall conductivity (SHC) tensor, which is one of the effects contributing to SCI. These calculations output zero values for tensor components not allowed by symmetry, such as σ_{yz}^{y}, while all components allowed by symmetry are nonzero [48]. Our DFT calculations yield a finite value for the nonorthogonal SHC component, σ_{zz}^{y}, which is symmetry allowed but predicted to be negligible in previous works [65]. Our calculations show that σ_{zz}^{y} is not negligible but does remain smaller than the other dominant components around the Fermi energy, such as σ_{zx}^{y}. Our experimental observation that $|\sigma_{zx}^{y}| \gg |\sigma_{zz}^{y}|$ is therefore consistent with a spin Hall contribution to these effects. Our calculations, however, predict opposite signs for these two components. Given the small value of σ_{zz}^{y}, a sign change is not implausible due to contributions from extrinsic effects, such as skew-scattering and/or EE SCI mechanisms, which can never be excluded from our observations and preclude quantitative comparisons with intrinsic SHC calculations.

IV. CONCLUSIONS

We perform SCI experiments in a graphene/$MoTe_2$ van der Waals heterostructure–based LSV, in both the standard and 3D-current configurations. Our measurement configurations allow access to three different SCI components enabled by the low resistance of the graphene/$MoTe_2$ interface. First, we confirm an unconventional SCI process, where a charge current applied along y generates spin polarization parallel to it, which can neither be explained by the SHE in $MoTe_2$ nor by the EE in proximitized graphene without further lowering the system's symmetry by shear strain or twisting between the layers. Also in the same device, we detect an orthogonal SCI component not experimentally observed before using LSVs, where the charge current applied along x generates spin polarization along y. As both the SHE in $MoTe_2$ and the EE in proximitized graphene allow this SCI configuration, either or both of them are plausible origins. Finally, we observe a third component of SCI, where charge current along z is parallel to the spin-current direction, with the spins polarized along y. This nonorthogonal component is allowed by the crystal symmetry of $1T'$-$MoTe_2$ and can only be attributed to the SHE in $MoTe_2$. To further confirm its origin, we perform DFT calculations, showing that this component is not only allowed by symmetry, but the intrinsic σ_{zz}^{y} is also nonzero. Considering all the above, a charge current in any direction within the graphene/$MoTe_2$ heterostructure generates spins polarized along the long axis of $MoTe_2$, which corresponds to the direction along the Mo-atom chain. Furthermore, when contributions from all three charge-current directions add up, the spin-polarization signal doubles the best value obtained for current flowing in only one direction. The rich spin-charge interconversion configurations in this system, with remarkable amplitude signals at room temperature, add flexibility to the architecture of next-generation spin-based devices.

ACKNOWLEDGMENTS

This work is supported by the Spanish MICINN under Projects No. RTI2018-094861-B-I00, No. PGC2018-101988-B-C21, No. PID2019-109905GB-C21, No. MAT 2017-88377-C2-2-R, and the Maria de Maeztu Units of Excellence Programme (Grants No. MDM-2016-0618 and

No. CEX2020-001038-M); the "Valleytronics" Intel Science Technology Center; the Gipuzkoa Regional Council under Projects No. 2021-CIEN-000037-01 and No. 2021-CIEN-000070-01; and the European Union H2020 under the Marie Sklodowska-Curie Actions (Grants No. 0766025-QuESTech and No. 794982-2DSTOP). N.O. thanks the Spanish MICINN for support from a Ph.D. fellowship (Grant No. BES-2017-07963). J.I.-A. acknowledges support from the "Juan de la Cierva-Formación" program by the Spanish MICINN (Grant No. FJC2018-038688-I) for a postdoctoral fellowship. R.C. acknowledges funding from Generalitat Valenciana through Grant No. CIDEGENT/2018/004 M.G.V. and I.R. thanks support from the Spanish MICINN (grant PID2019-109905GB-C21), the German Research Foundation DFG (grant nr. GA3314/1-1-FOR 5249 QUAST) and the European Research Council ERC (Grant No. 101020833).

[1] A. K. Geim and K. S. Novoselov, The rise of graphene, Nat. Mater. **6**, 183 (2007).

[2] A. K. Geim, Graphene: Status and prospects, Science **324**, 1530 (2009).

[3] A. K. Geim and I. V. Grigorieva, van der Waals heterostructures, Nature **499**, 419 (2013).

[4] S. Das, J. A. Robinson, M. Dubey, H. Terrones, and M. Terrones, Beyond graphene: Progress in novel two-dimensional materials and van der Waals solids, Annu. Rev. Mater. Res. **45**, 1 (2015).

[5] Y. Liu, N. O. Weiss, X. Duan, H.-C. Cheng, Y. Huang, and X. Duan, van der Waals heterostructures and devices, Nat. Rev. Mater. **1**, 16042 (2016).

[6] S. Manzeli, D. Ovchinnikov, D. Pasquier, O. V. Yazyev, and A. Kis, 2D transition metal dichalcogenides, Nat. Rev. Mater. **2**, 17033 (2017).

[7] C. S. Lian, C. Heil, X. Liu, C. Si, F. Giustino, and W. Duan, Coexistence of superconductivity with enhanced charge density wave order in the two-dimensional limit of $TaSe_2$, J. Phys. Chem. Lett. **10**, 4076 (2019).

[8] T. Li, S. Jiang, N. Sivadas, Z. Wang, Y. Xu, D. Weber, J. E. Goldberger, K. Watanabe, T. Taniguchi, C. J. Fennie, *et al.*, Pressure-controlled interlayer magnetism in atomically thin CrI_3, Nat. Mater. **18**, 1303 (2019).

[9] A. Hamill, B. Heischmidt, E. Sohn, D. Shaffer, K.-T. Tsai, X. Zhang, X. Xi, A. Suslov, H. Berger, Forró László, *et al.*, Two-fold symmetric superconductivity in few-layer $NbSe_2$, Nat. Phys. **17**, 949 (2021).

[10] T. Knobloch, Y.Yu Illarionov, F. Ducry, C. Schleich, S. Wachter, K. Watanabe, T. Taniguchi, T. Mueller, M. Walt, M. Lanza, *et al.*, The performance limits of hexagonal boron nitride as an insulator for scaled CMOS devices based on two-dimensional materials, Nat. Electron. **4**, 98 (2021).

[11] N. Tombros, C. Jozsa, M. Popinciuc, H. T. Jonkman, and B. J. van Wees, Electronic spin transport and spin precession in single graphene layers at room temperature, Nature **448**, 571 (2007).

[12] J. Ingla-Aynés, M. H. D. Guimarães, R. J. Meijerink, P. J. Zomer, and B. J. van Wees, 24-μm spin relaxation length in boron nitride encapsulated bilayer graphene, Phys. Rev. B **92**, 201410(R) (2015).

[13] M. Drögeler, C. Franzen, F. Volmer, T. Pohlmann, L. Banszerus, M. Wolter, K. Watanabe, T. Taniguchi, C. Stampfer, and B. Beschoten, Spin lifetimes exceeding 12 ns in graphene nonlocal spin valve devices, Nano Lett. **16**, 3533 (2016).

[14] J. Ingla-Aynés, R. J. Meijerink, and B. J. van Wees, Eighty-eight percent directional guiding of spin currents with 90 μm relaxation length in bilayer graphene using carrier drift, Nano Lett. **16**, 4825 (2016).

[15] M. Gmitra and J. Fabian, Graphene on transition-metal dichalcogenides: A platform for proximity spin-orbit physics and optospintronics, Phys. Rev. B **92**, 155403 (2015).

[16] M. Gmitra, D. Kochan, P. Högl, and J. Fabian, Trivial and inverted Dirac bands and the emergence of quantum spin Hall states in graphene on transition-metal dichalcogenides, Phys. Rev. B **93**, 155104 (2016).

[17] J. H. Garcia, A. W. Cummings, and S. Roche, Spin Hall effect and weak antilocalization in graphene/transition metal dichalcogenide heterostructures, Nano Lett. **17**, 5078 (2017).

[18] M. Offidani, M. Milletarì, R. Raimondi, and A. Ferreira, Optimal Charge-to-Spin Conversion in Graphene on Transition-Metal Dichalcogenides, Phys. Rev. Lett. **119**, 196801 (2017).

[19] J. H. Garcia, M. Vila, A. W. Cummings, and S. Roche, Optimal charge-to-spin conversion in graphene on transition-metal dichalcogenides, Chem. Soc. Rev. **47**, 3359 (2018).

[20] I. Žutić, A. Matos-Abiague, B. Scharf, H. Dery, and K. Belashchenko, Proximitized materials, Mater. Today **22**, 85 (2019).

[21] Z. Wang, D. Ki, H. Chen, H. Berger, A. H. MacDonald, and A. F. Morpurgo, Strong interface-induced spin–orbit interaction in graphene on WS_2, Nat. Commun. **6**, 8339 (2015).

[22] B. Yang, M.-F. Tu, J. Kim, Y. Wu, H. Wang, J. Alicea, R. Wu, M. Bockrath, and J. Shi, Tunable spin–orbit coupling and symmetry-protected edge states in graphene/WS_2, 2D Mater. **3**, 031012 (2016).

[23] S. Zihlmann, A. W. Cummings, J. H. Garcia, M. Kedves, K. Watanabe, T. Taniguchi, C. Schönenberger, and P. Makk, Large spin relaxation anisotropy and valley-Zeeman spin-orbit coupling in WSe_2/graphene/h-BN heterostructures, Phys. Rev. B **97**, 075434 (2018).

[24] T. Wakamura, F. Reale, P. Palczynski, S. Guéron, C. Mattevi, and H. Bouchiat, Strong Anisotropic Spin-Orbit Interaction Induced in Graphene by Monolayer WS_2, Phys. Rev. Lett. **120**, 106802 (2018).

[25] B. Yang, E. Molina, J. Kim, D. Barroso, M. Lohmann, Y. Liu, Y. Xu, R. Wu, L. Bartels, K. Watanabe, T. Taniguchi, and J. Shi, Effect of distance on photoluminescence quenching and proximity-induced spin–orbit coupling in graphene/WSe_2 heterostructures, Nano Lett. **18**, 3580 (2018).

[26] T. S. Ghiasi, J. Ingla-Aynés, A. A. Kaverzin, and B. J. van Wees, Large proximity-induced spin lifetime anisotropy in transition-metal dichalcogenide/graphene heterostructures, Nano Lett. **17**, 7528 (2017).

[27] L. A. Benítez, J. F. Sierra, W. Savero Torres, A. Arrighi, F. Bonell, M. v. Costache, and S. O. Valenzuela, Strongly

anisotropic spin relaxation in graphene–transition metal dichalcogenide heterostructures at room temperature, Nat. Phys. **14**, 303 (2017).

[28] A. W. Cummings, J. H. Garcia, J. Fabian, and S. Roche, Giant Spin Lifetime Anisotropy in Graphene Induced by Proximity Effects, Phys. Rev. Lett. **119**, 206601 (2017).

[29] W. Yan, O. Txoperena, R. Llopis, H. Dery, L. E. Hueso, and F. Casanova, A two-dimensional spin field-effect switch, Nat. Commun. **7**, 13372 (2016).

[30] A. Dankert and S. P. Dash, Electrical gate control of spin current in van der Waals heterostructures at room temperature, Nat. Commun. **8**, 16093 (2017).

[31] J. Ingla-Aynés, F. Herling, J. Fabian, L. E. Hueso, and F. Casanova, Electrical Control of Valley-Zeeman Spin-Orbit-Coupling–Induced Spin Precession at Room Temperature, Phys. Rev. Lett. **127**, 047202 (2021).

[32] C. K. Safeer, J. Ingla-Aynés, F. Herling, J. H. Garcia, M. Vila, N. Ontoso, M. R. Calvo, S. Roche, L. E. Hueso, and F. Casanova, Room-temperature spin Hall effect in graphene/MoS_2 van der Waals heterostructures, Nano Lett. **19**, 1074 (2019).

[33] F. Herling, C. K. Safeer, J. Ingla-Aynés, N. Ontoso, L. E. Hueso, and F. Casanova, Gate tunability of highly efficient spin-to-charge conversion by spin Hall effect in graphene proximitized with WSe_2, APL Mater. **8**, 071103 (2020).

[34] T. S. Ghiasi, A. A. Kaverzin, P. J. Blah, and B. J. van Wees, Charge-to-spin conversion by the Rashba–Edelstein effect in two-dimensional van der Waals heterostructures up to room temperature, Nano Lett. **19**, 5959 (2019).

[35] L. A. Benítez, W. Savero Torres, J. F. Sierra, M. Timmermans, J. H. Garcia, S. Roche, M. v. Costache, and S. O. Valenzuela, Tunable room-temperature spin galvanic and spin Hall effects in van der Waals heterostructures, Nat. Mater. **19**, 170 (2020).

[36] L. Li, J. Zhang, G. Myeong, W. Shin, H. Lim, B. Kim, S. Kim, T. Jin, S. Cavill, B. S. Kim, *et al.*, Gate-tunable reversible Rashba–Edelstein effect in a few-layer graphene/$2H$-TaS_2 heterostructure at room temperature, ACS Nano **14**, 5251 (2020).

[37] D. Khokhriakov, A. M. Hoque, B. Karpiak, and S. P. Dash, Gate-tunable spin-galvanic effect in graphene-topological insulator van der Waals heterostructures at room temperature, Nat. Commun. **11**, 3657 (2020).

[38] A. Md. Hoque, D. Khokhriakov, B. Karpiak, and S. P. Dash, Charge-spin conversion in layered semimetal $TaTe_2$ and spin injection in van der Waals heterostructures, Phys. Rev. Res. **2**, 033204 (2020).

[39] A. Md. Hoque, D. Khokhriakov, K. Zollner, B. Zhao, B. Karpiak, J. Fabian, and S. P. Dash, All-electrical creation and control of spin-galvanic signal in graphene and molybdenum ditelluride heterostructures at room temperature, Commun. Phys. **4**, 124 (2021).

[40] A. Manchon, J. Železný, I. M. Miron, T. Jungwirth, J. Sinova, A. Thiaville, K. Garello, and P. Gambardella, Current-induced spin-orbit torques in ferromagnetic and antiferromagnetic systems, Rev. Mod. Phys. **91**, 035004 (2019).

[41] S. Manipatruni, D. E. Nikonov, C.-C. Lin, T. A. Gosavi, H. Liu, B. Prasad, Y.-L. Huang, E. Bonturim, R. Ramesh, and I. A. Young, Scalable energy-efficient magnetoelectric spin–orbit logic, Nature **565**, 35 (2018).

[42] V. T. Pham, I. Groen, S. Manipatruni, W. Y. Choi, D. E. Nikonov, E. Sagasta, C.-C. Lin, T. A. Gosavi, A. Marty, L. E. Hueso, *et al.*, Spin–orbit magnetic state readout in scaled ferromagnetic/heavy metal nanostructures, Nat. Electron. **3**, 309 (2020).

[43] D. Culcer and R. Winkler, Generation of Spin Currents and Spin Densities in Systems with Reduced Symmetry, Phys. Rev. Lett. **99**, 226601 (2007).

[44] M. Seemann, D. Ködderitzsch, S. Wimmer, and H. Ebert, Symmetry-imposed shape of linear response tensors, Phys. Rev. B **92**, 155138 (2015).

[45] Y. Zhang, Q. Xu, K. Koepernik, J. Železný, T. Jungwirth, C. Felser, J. van den Brink, and Y. Sun, Different types of spin currents in the comprehensive materials database of nonmagnetic spin Hall effect, npj Comput. Mater. **7**, 167 (2021).

[46] A. Roy, M. H. D. Guimarães, and J. Slawinska, Unconventional spin Hall effects in nonmagnetic solids, Phys. Rev. Mater. **6**, 045004 (2022).

[47] W. G. Dawson and D. W. Bullett, Electronic structure and crystallography of $MoTe_2$ and WTe_2, J. Phys. C: Solid State Phys. **20**, 61594174 (1987).

[48] See the Supplemental Material at http://link.aps.org/supplemental/10.1103/PhysRevApplied.19.014053 for DFT calculations of all symmetry-allowed SHE tensor components for $MoTe_2$ (Sec. S1), characterization of $MoTe_2$ flakes with polarized Raman spectroscopy (Sec. S2), and spin Hanle measurements (Sec. S3), which also includes Refs. [72–82].

[49] C. G. Péterfalvi, A. David, P. Rakyta, G. Burkard, and A. Kormányos, Quantum interference tuning of spin-orbit coupling in twisted van der Waals trilayers, Phys. Rev. Res. **4**, L022049 (2022).

[50] A. Veneri, D. T. S. Perkins, C. G. Péterfalvi, and A. Ferreira, Twist angle controlled collinear Edelstein effect in van der Waals heterostructures, Phys. Rev. B **106**, L081406 (2022).

[51] T. Naimer, K. Zollner, M. Gmitra, and J. Fabian, Twist-angle dependent proximity induced spin-orbit coupling in graphene/transition metal dichalcogenide heterostructures, Phys. Rev. B **104**, 195156 (2021).

[52] A. David, P. Rakyta, A. Kormányos, and G. Burkard, Induced spin-orbit coupling in twisted graphene–transition metal dichalcogenide heterobilayers: Twistronics meets spintronics, Phys. Rev. B **100**, 085412 (2019).

[53] Y. Li and M. Koshino, Twist-angle dependence of the proximity spin-orbit coupling in graphene on transition-metal dichalcogenides, Phys. Rev. B **99**, 075438 (2019).

[54] S. Lee, D. J. P. de Sousa, Y.-K. Kwon, F. de Juan, Z. Chi, F. Casanova, and T. Low, Charge-to-spin conversion in twisted graphene/WSe_2 heterostructures, Phys. Rev. B **106**, 165420 (2022).

[55] C. K. Safeer, N. Ontoso, J. Ingla-Aynés, F. Herling, V. T. Pham, A. Kurzmann, K. Ensslin, A. Chuvilin, I. Robredo, M. G. Vergniory, *et al.*, Large multidirectional spin-to-charge conversion in low-symmetry semimetal $MoTe_2$ at room temperature, Nano Lett. **19**, 8758 (2019).

[56] L. Camosi, J. Světl, M. V. Costache, W. Savero Torres, I. Fernández Aguirre, V. Marinova, D. Dimitrov, M. Gospodinov, J. F. Sierra, and S. O. Valenzuela, Resolving spin currents and spin densities generated by charge-spin

interconversion in systems with reduced crystal symmetry, 2D Mater. **9**, 035014 (2022).

[57] J. Ingla-Aynés, I. Groen, F. Herling, N. Ontoso, C. K. Safeer, F. de Juan, L. E. Hueso, M. Gobbi, and F. Casanova, Omnidirectional spin-to-charge conversion in graphene/$NbSe_2$ van der Waals heterostructures, 2D Mater. **9**, 045001 (2022).

[58] G. M. Stiehl, R. Li, V. Gupta, I. E. Baggari, S. Jiang, H. Xie, L. F. Kourkoutis, K. F. Mak, J. Shan, R. A. Buhrman, and D. C. Ralph, Layer-dependent spin-orbit torques generated by the centrosymmetric transition metal dichalcogenide β-$MoTe_2$, Phys. Rev. B **100**, 184402 (2019).

[59] P. Song, C. H. Hsu, G. Vignale, M. Zhao, J. Liu, Y. Deng, W. Fu, Y. Liu, Y. Zhang, H. Lin, *et al.*, Coexistence of large conventional and planar spin Hall effect with long spin diffusion length in a low-symmetry semimetal at room temperature, Nat. Mater. **19**, 292 (2020).

[60] B. Zhao, B. Karpiak, D. Khokhriakov, A. Johansson, A. M. Hoque, X. Xu, Y. Jiang, I. Mertig, and S. P. Dash, Unconventional charge–spin conversion in Weyl-semimetal WTe_2, Adv. Mater. **32**, 2000818 (2020).

[61] Z. Zoltán, K. Kovács-Krausz, A. M. Hoque, P. Makk, B. S. Szentpéteri, M. Mátyá, M. Kocsis, B. Fü, M. V. Yakushev, T. V. Kuznetsova, *et al.*, Electrically controlled spin injection from giant Rashba spin–orbit conductor BiTeBr, Nano Lett. **20**, 4782 (2020).

[62] A. Castellanos-Gomez, M. Buscema, R. Molenaar, V. Singh, L. Janssen, H. S. J. van der Zant, and G. A. Steele, Deterministic transfer of two-dimensional materials by all-dry viscoelastic stamping, 2D Mater. **1**, 011002 (2014).

[63] Y. Deng, X. Zhao, C. Zhu, P. Li, R. Duan, G. Liu, and Z. Liu, $MoTe_2$: Semiconductor or semimetal?, ACS Nano **15**, 12465 (2021).

[64] K. Zhang, C. Bao, Q. Gu, X. Ren, H. Zhang, K. Deng, Y. Wu, Y. Li, J. Feng, and S. Zhou, Raman signatures of inversion symmetry breaking and structural phase transition in type-II Weyl semimetal $MoTe_2$, Nat. Commun. **7**, 13552 (2016).

[65] R. He, S. Zhong, H. H. Kim, G. Ye, Z. Ye, L. Winford, D. McHaffie, I. Rilak, F. Chen, X. Luo, *et al.*, Dimensionality-driven orthorhombic $MoTe_2$ at room temperature, Phys. Rev. B **97**, 041410(R) (2018).

[66] . A. Md. Hoque, B. Zhao, D. Khokhriakov, P. Muduli, and S. P. Dash, ArXiv: 2205.08327 (2022).

[67] B. Zhao, A. Md. Hoque, D. Khokhriakov, B. Karpiak, and S. P. Dash, Charge-spin conversion signal in WTe_2 van der Waals hybrid devices with a geometrical design, Appl. Phys. Lett. **117**, 242401 (2020).

[68] B. Zhao, D. Khokhriakov, Y. Zhang, H. Fu, B. Karpiak, A. M. Hoque, X. Xu, Y. Jiang, B. Yan, and S. P. Dash, Observation of charge to spin conversion in Weyl semimetal WTe_2 at room temperature, Phys. Rev. Res. **2**, 013286 (2020).

[69] W. Yan, E. Sagasta, M. Ribeiro, Y. Niimi, L. E. Hueso, and F. Casanova, Large room temperature spin-to-charge conversion signals in a few-layer graphene/Pt lateral heterostructure, Nat. Commun. **8**, 661 (2017).

[70] S. O. Valenzuela and M. Tinkham, Direct electronic measurement of the spin Hall effect, Nature **442**, 176 (2006).

[71] N. J. G. Couto, D. Costanzo, S. Engels, D.-K. Ki, K. Watanabe, T. Taniguchi, C. Stampfer, F. Guinea, and A. F. Morpurgo, Random Strain Fluctuations as Dominant Disorder Source for High-Quality On-Substrate Graphene Devices, Phys. Rev. X **4**, 041019 (2014).

[72] G. Kresse and J. Hafner, *Ab initio* molecular dynamics for liquid metals, Phys. Rev. B **47**, 558 (1993).

[73] G. Kresse and J. Hafner, *Ab initio* molecular-dynamics simulation of the liquid-metal, Phys. Rev. B **49**, 14251 (1994).

[74] G. Kresse and J. Furthmuller, Efficiency of *ab-initio* total energy calculations for metals and semiconductors using a plane-wave basis set, Comput. Mater. Sci. **6**, 15 (1996).

[75] G. Kresse and J. Furthmuller, Efficient iterative schemes for *ab initio* total-energy calculations using a plane-wave basis set, Phys. Rev. B **54**, 11169 (1996).

[76] G. Kresse and D. Joubert, From ultrasoft pseudopotentials to the projector augmented-wave method, Phys. Rev. B **59**, 1758 (1999).

[77] J. P. Perdew, K. Burke, and M. Ernzerhof, Generalized Gradient Approximation Made Simple, Phys. Rev. Lett. **77**, 3865 (1996).

[78] D. Hobbs, G. Kresse, and J. Hafner, Fully unconstrained noncollinear magnetism within the projector augmented-wave method, Phys. Rev. B **62**, 11556 (2000).

[79] G. Pizzi, *et al.*, Wannier90 as a community code: New features and applications, J. Phys.: Condens. Matter **32**, 165902 (2020).

[80] S. S. Tsirkin, High performance Wannier interpolation of Berry curvature and related quantities with WannierBerri code, npj Comput. Mater. **7**, 33 (2021).

[81] S.-Y. Chen, T. Goldstein, D. Venkataraman, A. Ramasubramaniam, and J. Yan, Activation of new Raman modes by inversion symmetry breaking in type II Weyl semimetal candidate T'-$MoTe_2$, Nano Lett. **16**, 5852 (2016).

[82] C. K. Safeer, F. Herling, W. Y. Choi, N. Ontoso, J. Ingla-Aynés, L. E Hueso and F. Casanova, Reliability of spin-to-charge conversion measurements in graphene-based lateral spin valves, 2D Mater. **9**, 015024 (2022).